14D.1 TROPICAL CYCLONE DETECTIONS AND SEASONAL GENESIS VARIABLES IN ECMWF REANALYSIS DATA

K. Tory[1], H. Ye and R. Dare

Research and Development, Australian Bureau of Meteorology

1. INTRODUCTION

Over the last decade climate model studies have provided an increasingly consistent message that global numbers of tropical cyclones (TC) will decrease in a warming world (e.g., Knutson et al. 2010, Walsh et al. 2015). Regional projections are less certain due to model limitations in generating realistic climatologies of TC-like circulations, and our ability to accurately detect them (e.g., Tory et al. 2013b,c). This uncertainty coupled with large natural variability within basins can make it difficult to identify a signal of change in TC formation on basin-wide and smaller spatial scales, especially in regions where TC formation is relatively infrequent in the current climate.

An understanding of why TCs form where they do in the real atmosphere and in climate models, and whether the reasons are consistent, is important for understanding errors in model TC formation location and timing, and will help identify whether climate models are producing TCs for the right reason. However, the very large number of models and scenarios to be investigated makes it difficult to perform in-depth analyses to identify why these variables change in different climate scenarios.

In this study we present simple diagnostics that provide an indication of TC formation favourability that can be illustrated in one or two summary images. These quantities define regions of TC favourability, consistent with the detected TCs, and provide insight into the tropical circulation responsible for the TC distribution.

Our search for seasonally averaged variables that influence global TC formation distributions identified a potentially useful new ingredient for TC genesis indices: the meridional gradient of absolute vorticity (β^*).

We consider threshold values of the seasonally averaged variables to define geographic TC formation distributions, rather than the genesis index approach that uses complex mathematical functions of these variables to define TC formation densities (e.g., Emanuel and Nolan 2004, Emanuel 2010, Tippet et al. 2011, Korty et al. 2012a,b, Bruyere et al. 2012). Additional useful information is obtained by considering separately thresholds that define tropical depression (TD) formation distributions, and regions in which a large proportion of TDs become tropical storms (TSs, i.e., storms that exceed gale force intensity). Knowledge of the threshold quantities responsible for these boundaries at any particular geographic location provides useful insight into what supports and inhibits TD or TS formation there.

With future applications to climate models in mind, the thresholds are constructed around detected distributions of TDs and TSs rather than observed storm distributions. This ensures greater consistency between the threshold/storm relationship developed in reanalysis data and its application to climate model data.

In the next section the OWZP detection method is described, the new genesis index ingredient, and the threshold variables used are introduced. In Section 3 the TD threshold application and distribution is described and illustrated, and the significance of the results presented in Section 4. Section 5 contains a brief description of an additional set of thresholds used to define regions where a high proportion of TDs transition to TSs. The work is summarised in Section 6.

2. METHODOLOGY

2.1 *OWZP detections*

TDs and TSs are detected using the OWZP TC detection scheme (Tory et al. 2013a—d), which identifies regions favourable for TC formation in instantaneous data on the scale of about 1000 km. This includes thresholds of thermodynamic variables, wind shear, and a measure of the rotational background flow identified in the OWZ quantity,

$$OWZ = sgn(f) \times (\zeta + f) \times max\left[\frac{\zeta^2 - (E^2 + F^2)}{\zeta^2}, 0\right] \quad 1.$$

Here f is Coriolis, ζ is relative vorticity, $E = u_x - v_y$ the stretching deformation, $F = v_x + u_y$ the shearing deformation, and the subscripts x and

y represent zonal and meridional gradients respectively. The term is multiplied by the sign of f to ensure positive values for cyclonic flow in both hemispheres. Only positive values of the normalized OW (the term inside the square brackets of Eq. 1) are included, so that OWZ ranges from 1 for solid body rotation to zero when deformation exceeds vorticity. Thus, the OWZ is essentially the absolute vorticity scaled by the degree of deformation in the flow (e.g., OWZ = 0 for shear vorticity, and OWZ = $\zeta + f$ = absolute vorticity (η) for solid body rotation).

The combined thermodynamic, shear and OWZ thresholds describe conditions favourable for TC formation. When the conditions have been favourable for at least 24 and 48 hours respectively, a TD and TS are deemed to have formed. Applied to ERA-interim reanalysis data and verified against observed TSs (IBTrACS, Knapp et al. 2010), the OWZP global performance includes a "hit" rate of about 80% and "false alarm" rate of about 20% (e.g., Tory et al. 2013d).

2.2 *A new genesis index ingredient:* β^*

Many recognised and potential genesis index ingredients, plus numerous variants, were investigated here as potential threshold indices. Candidates included the meridional gradient of absolute vorticity,

$$\beta^* = \frac{\partial \eta}{\partial y} = \frac{\partial f}{\partial y} + \frac{\partial \zeta}{\partial y}, \qquad 2.$$

in an attempt to capture the contribution to genesis from barotropic instability (or weak barotropic stability). Seasonally averaged values are presented in Fig. 1 for the summer seasons, with the locations of observed TSs overlayed. There is a clear preference for TC formation in regions of small β^*, and an almost complete formation absence in regions of large β^*. This suggests β^* has potential to be a useful seasonal genesis index ingredient.

2.3 *Seasonal threshold variables*

Threshold values were chosen subjectively, by looking for values that included the majority of the detected TDs. Of the many seasonal threshold variables considered, the most valuable were those used in typical genesis indices:

1. Middle-troposphere relative humidity (RH_{700});
2. Potential intensity (V_{PI}, e.g., Bister and Emanuel 1998, 2002);
3. The magnitude of the difference in vector winds between the 200 and 850 hPa pressure levels (V_{sh}).

and a hybrid variable;

4. The cyclonic absolute vorticity divided by a normalised β^*,

$$\xi = \frac{|\eta|_{850}}{\beta^*_{700}(R/2\Omega)}. \qquad 3.$$

Here R and Ω, the earth radius and rotation frequency, are used to normalise β^* to give ξ the same units as η. The subscripts represent the pressure levels in hPa.

3. THRESHOLD APPLICATION

The choice of threshold variables, and values was decided from a subjective assessment of a wide range of quantities known to influence TC formation. Each quantity was averaged over 3-month periods (Jan—Mar, Apr—Jun, Jul—Sep, Oct—Dec) for the 34 year period 1979—2013, and also separated into El Nino, La Nina and neutral years, and overlayed with OWZP TD and TS detections relevant to each period. The main aim was to identify fundamental quantities that define the geographical boundaries of TD formation. Large variability of some quantities in the transition seasons of Spring and Autumn meant that the main focus had to be on the more stable summer and winter seasons. The subjective assessment of each quantity was first tested for all years, and the sensitivity to ENSO variability was used to fine tune the choice of thresholds. Only four variables were required to define the TD formation boundaries. It was found that ξ and V_{PI} essentially represent kinematic and thermodynamic potential for TC formation, and that RH_{700} and V_{sh} can be considered quantities that inhibit development.

The $\xi = 2.0 \times 10^{-5} s^{-1}$, and $V_{PI} = 40\ ms^{-1}$ threshold contours are plotted in Fig. 2 for the summer seasons, with detected TDs and TSs overlayed. The two contours largely determine the equatorward and poleward TD formation boundaries respectively. The V_{PI} threshold has much in common with Palmén (1948) and Gray's (1968) sea-surface temperature (SST) thresholds, due to the strong influence of SST on V_{PI} (e.g., Polvani et al. 2016). As in Gray's analysis there are regions during the summer seasons with apparent thermodynamic potential, but no TC formation (e.g., parts of the SE Pacific, S Atlantic, central N Pacific and central

N Atlantic, Fig. 2). Interestingly, large tracts of the winter tropics show thermodynamic potential (indicated by $V_{PI} > 40\ ms^{-1}$, Fig. 2) with no evidence of TD formation. Clearly, other atmospheric variables limit TD formation in these regions.

The $RH_{700} = 40\%$ threshold is added to the ξ and V_{PI} thresholds in Fig. 3. This eliminates most of the regions with favourable V_{PI} and no TD formation, mentioned above. The remaining exceptions are the Northern winter, western hemisphere ITCZ, the N Indian Ocean during the monsoon season (where V_{sh} is known to be excessive) and part of the winter S Pacific, between about 150° and 200° E, and 5° and 10° S. The inclusion of the $V_{sh} = 25\ ms^{-1}$ threshold (Fig. 4) eliminates the N Indian ocean monsoon region and the winter ITCZ mentioned above, but not the winter S Pacific region.

A summary plot of favourable TD formation regions that incorporates all four threshold quantities is provided in Fig. 5. This figure shows that a small fraction of detected TDs and TSs fall outside the TD formation boundaries. Some of these storms can be explained by ENSO variations in the boundary locations, and some of the higher latitude detections are known to be sub-tropical or mid-latitude storms that were not correctly identified as such, and then eliminated, by the objective subtropical jet analysis, which we use to define the edge of the tropics. Other examples are likely to be formations in regions with high temporal variability in some of the threshold quantities (e.g., short periods of weak shear exist in locations where the seasonal average is high).

4. SIGNIFICANCE OF RESULTS

Active convective regions have high β^* on the equatorward side of the convective maximum (cf. Figs 1 and 6) and reduced cyclonic η from cross equatorial η—advection (not shown). Both contribute to unfavourable TC formation conditions characterised by small ξ (Eq. 3), which shifts the favourable formation boundary away from the equator (Fig. 2). In the opposite hemisphere, the cross-equatorial flow provides an equatorward η—advection that enhances cyclonic η near the equator, which allows near-equator TD formation, provided other conditions are also favourable (e.g., NW Pacific basin, Fig. 2b, and S Indian basin, Fig. 2a).

V_{PI} is strongly influenced by the relative distribution of SST throughout the tropics (e.g., Vecchi and Soden 2007). The anticyclonic ocean gyres that dominate all ocean basins, except the N Indian, are largely responsible for the relative SST distributions, with equatorward cold water advection and cool upwelling in the eastern basin regions and poleward warm water advection in the west. As a consequence the $V_{PI} = 40\ ms^{-1}$ threshold generally extends further polewards (equatorwards) in the western (eastern) ocean basins, especially in the warm season (Fig. 2).

While ξ and V_{PI} largely determine the kinematic and thermodynamic potential for TD formation, it is the dry middle troposphere that inhibits formation in much of the winter hemispheres, the SE Pacific and most of the S Atlantic (Fig. 3). High wind shear has been blamed for the lack of formation in the SE Pacific and S Atlantic (e.g., Gray 1968), however our analysis shows that large parts of these two ocean basins experience favourable seasonally averaged wind shear (Fig. 7), whereas the entire SE Pacific and those parts of the S Atlantic where TDs do not form, experience a dry middle-troposphere (Fig. 8). Thus we conclude the primary TD formation inhibitor, globally, is low RH rather than wind shear. This conclusion is supported by the existence of high TC formation rates in the SW of the NW Pacific basin, where relatively high values of seasonally averaged shear (15—20 ms^{-1}) is widespread (Fig. 7a). A regional exception is the winter N Atlantic and NE Pacific, where the lack of formation could be attributed to excessive shear alone (Figs. 4b, 7b).

5. RECENT WORK

Work is underway to identify an additional set of thresholds that define a more favourable TS formation environment. For example, Fig. 9 shows the annual TD and TS distributions in each basin with the fraction of TDs that do not become TSs (TD failure rate) poleward and equatorward of a specified dividing latitude (25° in the NW Pacific, and 15° in all other basins). Fig. 9 shows a TD failure rate on the poleward side of the dividing lines almost double that on the equatorward side in all basins except the NE Pacific and the S Indian. These two basins have the majority of TC formations at relatively low latitudes. The higher latitudes in general

experience lower values of V_{PI} and/or higher wind shear, which make intensification to TS less favourable. (In the N Indian basin TD landfall is a major reason for TD failure poleward of the dividing latitude, due to the close proximity of land.)

The additional set of thresholds designed to identify regions of low TD failure rate, include combinations of V_{PI}, V_{sh} and β^*. This region is defined by wherever $V_{PI} > 65\ ms^{-1}$ and $V_{sh} < 10\ ms^{-1}$. However, the V_{sh} threshold is overridden wherever $V_{PI} > 75\ ms^{-1}$, and the V_{PI} threshold is overridden wherever $\beta^* < 0$. These threshold quantities are depicted in Fig. 10, and their combined implementation in defining the low TD failure regions is depicted by green contours in Fig. 11.

These results show that when a TD forms it is more likely to intensify further to a TS in regions of enhanced V_{PI} and reduced V_{sh}, which is consistent with all TC genesis index studies (e.g., Gray 1979, Royer et al 1998, Emanuel and Nolan 2004, Emanuel 2010, Tippet et al. 2011, Bruyere et al. 2012, Tang and Emanuel 2012, Korty et al. 2012a,b). The addition of the overriding $\beta^* < 0$ threshold only has value in the far eastern N Atlantic, where V_{PI} is relatively small, but there is a low TD failure rate. A comparison with observed TSs (Fig. 1a) suggest that the OWZP TS detection scheme identifies storms early here, in which case the β^* contribution may not be important for analysing observed TSs, although it may still be useful for analysing pre-TS storm formation.

6. SUMMARY

Despite steady improvements of TC formation climatologies in climate models over recent years, due largely to increasing model resolution, regional projections based on such models are subject to considerable uncertainty, even for relatively large regional scales (e.g., basin-wide). A better understanding of models strengths and weaknesses allows more informed projection conclusions. We are not aware of any detailed comparative studies of model performance across a range of models, presumably due to the significant effort required to analyse so many models. Thus, in this study we were motivated to derive a diagnostic tool that summarises TC formation model performance in a few simple images. The images describe the geographic distribution of TC formation, and the atmospheric variables that define the formation boundaries. Applied to climate models the images are expected to provide insight into the models' tropical circulation, given an understanding of the relationship between the tropical circulation and these boundaries.

The initial testing of a wide range of parameters found that the seasonally averaged meridional gradient of absolute vorticity, β^*, is likely to be a very useful, and perhaps a currently "missing" TC genesis index ingredient.

Four threshold quantities that defined global TD distributions were identified: the hybrid η and β^* parameter ξ (Eq. 3), defined the equatorward formation boundary and represented a kinematic formation potential. Emanuel's potential intensity (V_{PI}) largely defined the poleward formation boundary and represented a thermodynamic formation potential. A dry middle troposphere provided the most globally consistent explanation for non-formation, where the atmosphere was otherwise kinematically and thermodynamically favourable (e.g., much of the winter hemispheres and the S Atlantic and SE Pacific). Excessive wind shear also explains the non-formation in the NE Pacific and N Atlantic winter months.

Early results investigating thresholds that define regions of low TD failure rate (i.e., most TDs intensify further to TSs), found that elevated V_{PI} and weak to moderate wind shear was very favourable (consistent with genesis index studies). However, low TD failure can also occur in regions of: moderate- to high-shear where V_{PI} is further elevated; and relatively low V_{PI} where $\beta^* < 0$.

We anticipate that the application of these diagnostics to climate models will enable the above insight into TC formation to be extracted from the models, and provide an understanding of why the models produce TCs where they do, which should enable the generation of a range of plausible future TC formation scenarios.

References

Bister, M., and K. A. Emanuel, 1998: Dissipative heating and hurricane intensity. Meteor. Atmos. Phys., **65**, 233–240, doi:10.1007/BF01030791.

Bister, M., and K. A. Emanuel, 2002: Low frequency variability of tropical cyclone

potential intensity. 1. Interannual to interdecadal variability. J. Geophys. Res., **107**, 4801, doi:10.1029/2001JD000776.

Bruyere, C. L., G. J. Holland, and E. Towler, 2012: Investigating the use of a genesis potential index for tropical cyclones in the North Atlantic basin. *J. Clim.,* **25**, 8611–8626.

Emanuel, K. A. and D. S. Nolan, 2004: Tropical cyclone activity and the global climate system. Preprints, *26th Conf. on Hurricanes and Tropical Meteorology*, Miami, Fl, Amer. Meteor. Soc., 10A.2.

Emanuel, K. A., 2010: Tropical cyclone activity downscaled from NOAACIRES reanalysis, 1908–1958. J. Adv. Model. Earth Syst., 2 (1), doi:10.3894/JAMES.2010.2.1.

Gray, W. M. 1968: Global view of the origin of tropical disturbances and storms. *Mon. Wea. Rev.*, **96**, 669—700.

Gray, W. M., 1979: Hurricanes: Their formation, structure and likely role in the tropical circulation. Meteorology over the Tropical Oceans, D. B. Shaw, Ed., Royal Meteorological Society, 155–218.

Knapp, K. R., M. C. Kruk, D. H. Levinson, H. J. Diamond, and C. J. Neumann, 2010: The International Best Track Archieve for Climate Stewardship (IBTrACS) Unifying Tropical Cyclone Data. *Bull. Amer. Meteor. Soc.*, **91**, 363–376.

Knutson, T. R., J.L. McBride, J.-C. Chan, K. Emanuel, G. Holland, C. Landsea, I. Held, J.P. Kossin, A.K. Srivastava, and M. Sugi, 2010: Tropical cyclones and climate change. *Nature Geoscience*, **3**, 157-163.

Korty, R. L., S. J. Camargo, and J. Galewsky, 2012a: Tropical cyclone genesis factors in simulations of the Last Glacial Maximum. J. Climate, **25**, 4348–4365.

Korty, R. L., S. J. Camargo, and J. Galewsky, 2012b: Variations in tropical cyclone genesis factors in simulations of the Holocene epoch. J. Climate, **25**, 8196–8211.

Palmén, E. H., 1948: On the formation and structure of tropical cyclones. *Geophysica*, Helsinki, **3**, 26—38.

Polvani, L.M, S.J. Camargo, and R.R. Garcia, 2016. The importance of the Montreal Protocol in mitigating the potential intensity of tropical cyclones. Journal of Climate, 29, 2275-2289, doi: 10.1175/JCLI-D-15-0232.1.

Royer J-F, Chauvin F, Timbal B, Araspin P, Grimal D, 1998: A GCM study of the impact of greenhouse gas increase on the frequency of occurrence of tropical cyclones. *Climatic Change,* **38**, 307–343.

Tang, B and K. A. Emanuel, 2012: A ventilation index for tropical cyclones. *Bull. Amer. Meteor. Soc.*, **93**, 1901—1912. DOI:10.1175/BAMS-D-11-00165.1

Tippett, M. K., S. J. Camargo, and A. H. Sobel, 2011: A Poisson regression index for tropical cyclone genesis and the role of large-scale vorticity in genesis. J. Climate, 24, 2335–2357.

Tory, K.J., R. A. Dare, N. E. Davidson, J. L. McBride, and S. S. Chand, 2013a: The importance of low-deformation vorticity in tropical cyclone formation. *Atmos. Chem. Phys.* **13**, 2115–2132.

Tory, K. J., S. S. Chand, R. A. Dare, and J. L. McBride, 2013b: The development and assessment of a model-, grid- and basin independent tropical cyclone detection scheme. *J. Climate*, **26**, 5493-5507.

Tory, K. J., S. S. Chand, R. A. Dare, and J. L. McBride, 2013c: An assessment of a model-independent tropical cyclone detection procedure in selected CMIP3 global climate models. *J. Climate*, **26**, 5508-5522.

Tory, K.J., S. S. Chand, J. L. McBride, H. Ye, R. A. Dare, 2013d: Projected changes in late 21st century tropical cyclone frequency in thirteen coupled climate models from the Coupled Model Intercomparison Project Phase 5. *J. Clim.*, **26**, 9946—9959.

Vecchi G. A. and B. J. Soden, 2007b: Effect of remote sea surface temperature change on tropical cyclone potential intensity. *Nature* **450**,1066–1070.

Walsh, K. J. E., J. L. McBride, P. J. Klotzbach, S. Balachandran, S. J. Camargo, G. Holland, T. R. Knutson, J. P. Kossin, T-C. Lee, A. Sobel and M. Sugi, 2015: Tropical cyclones and climate change. *WIREs Clim. Change.* DOI: 10.1002/WCC.371.

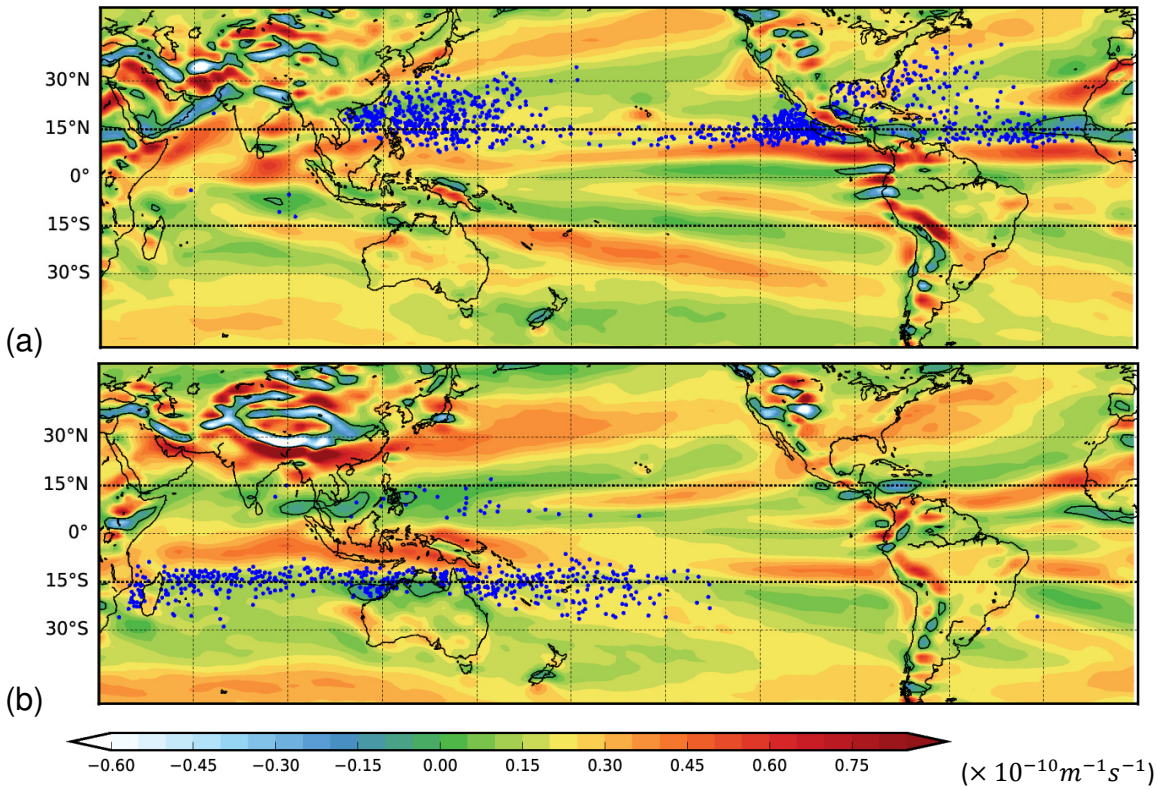

Figure 1: Summer season β^* on the 700 hPa pressure level with observed Tropical Storm formation locations (blue dots), for (a) July—September (b) January—March, from ECMWF reanalyses (1979—2013).

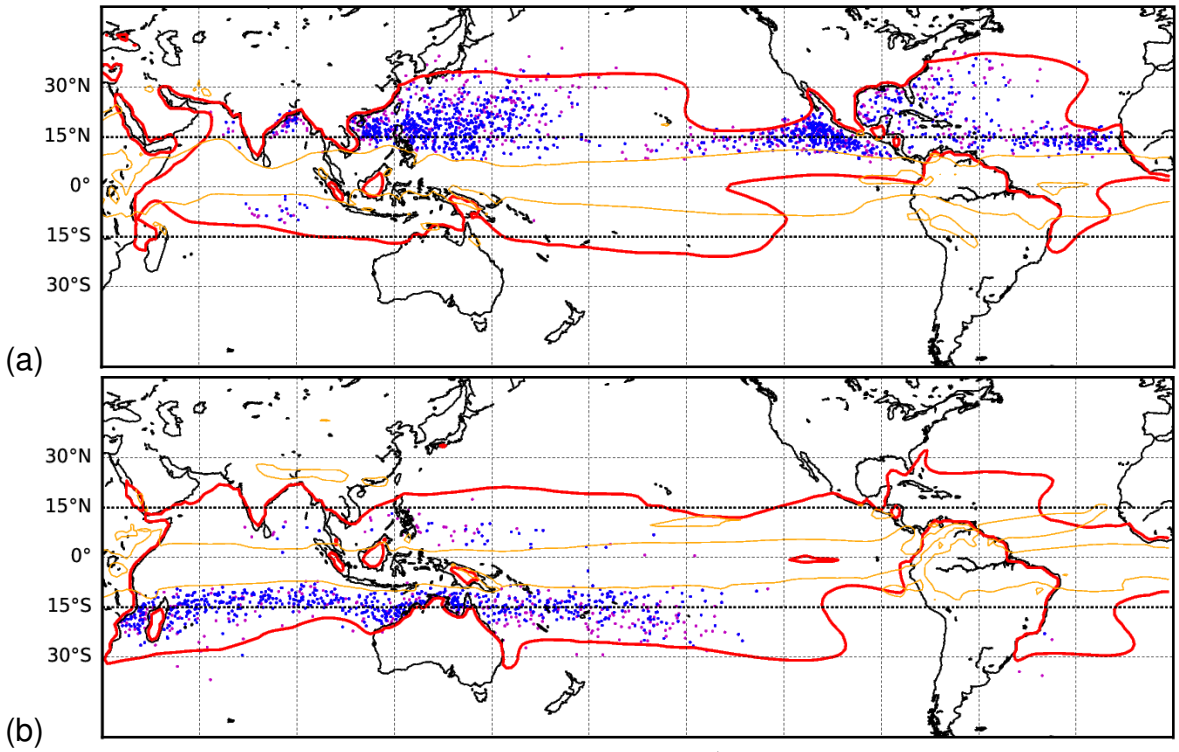

Figure 2: Summer season threshold contours of $\xi = 2.0 \times 10^{-5} s^{-1}$, (orange) and $V_{PI} = 40\ ms^{-1}$ (red), with OWZP detected TDs (purple dots) and TSs (blue dots), for (a) July—September (b) January—March, from ECMWF reanalysis data (1979—2013).

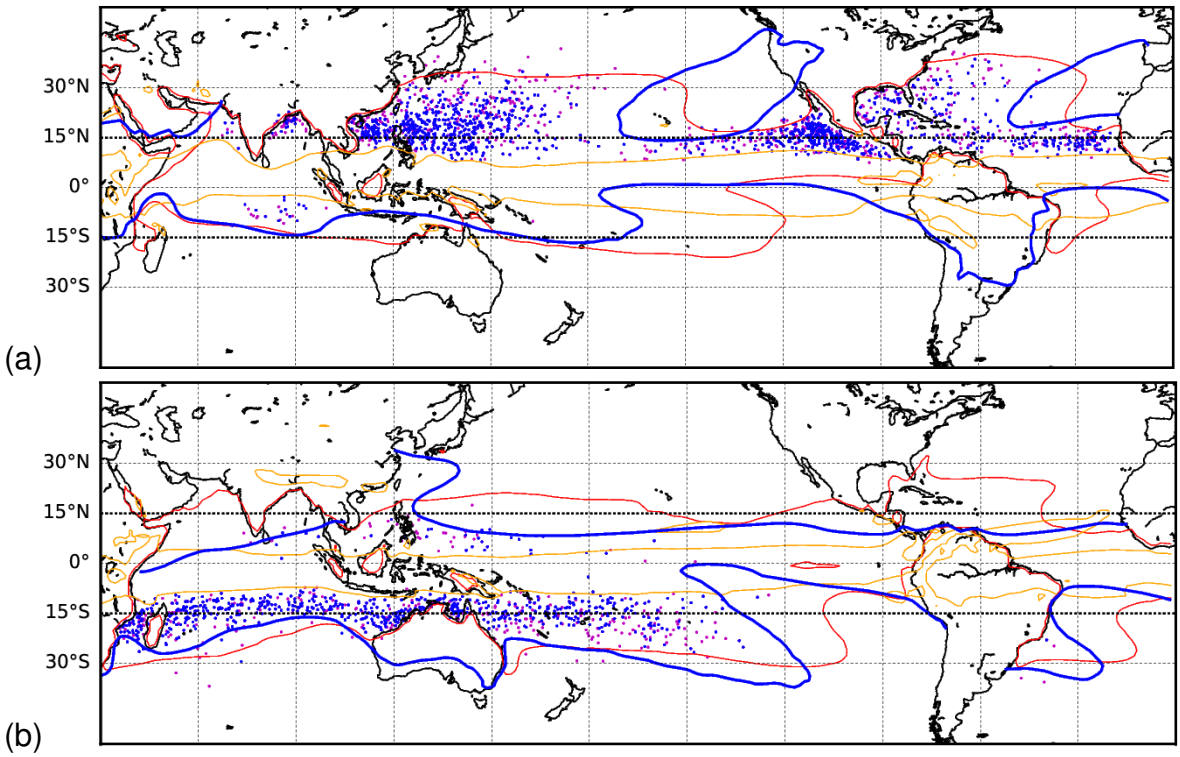

Figure 3: As in Fig. 2 but with threshold contours of $RH_{700} = 40\%$ (blue) added.

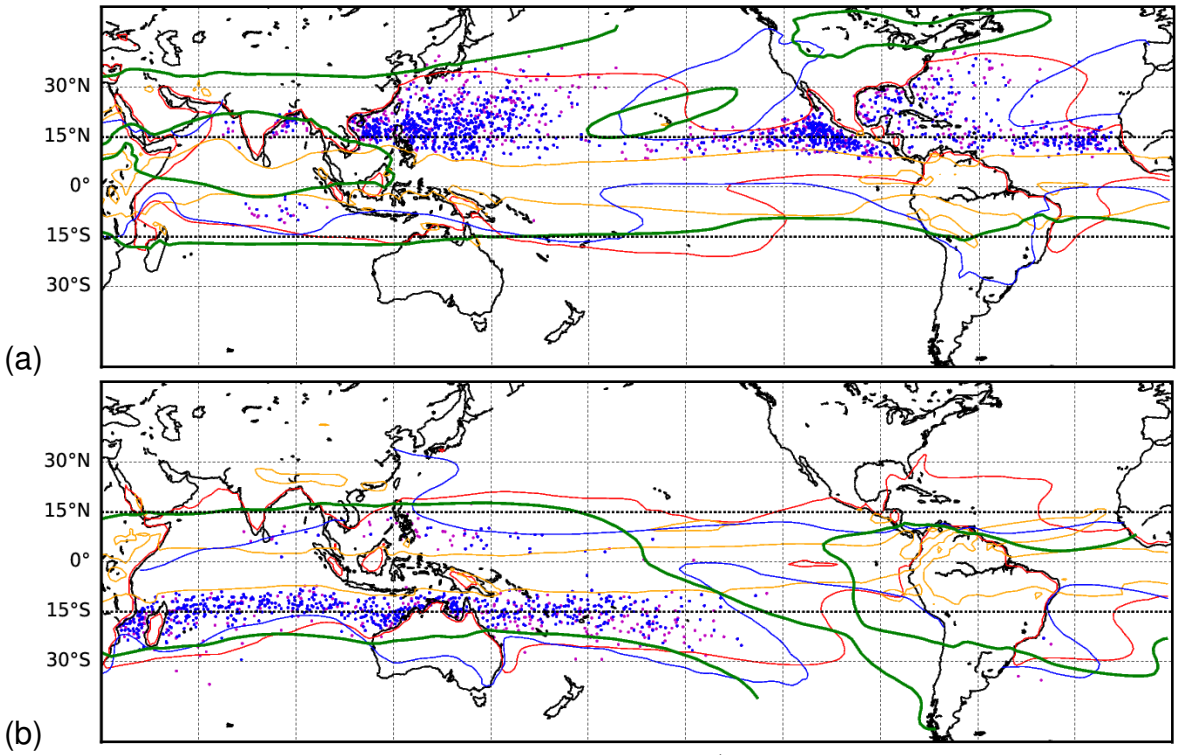

Figure 4: As in Fig. 3 but with threshold contours of $V_{sh} = 25\ ms^{-1}$ (green) added.

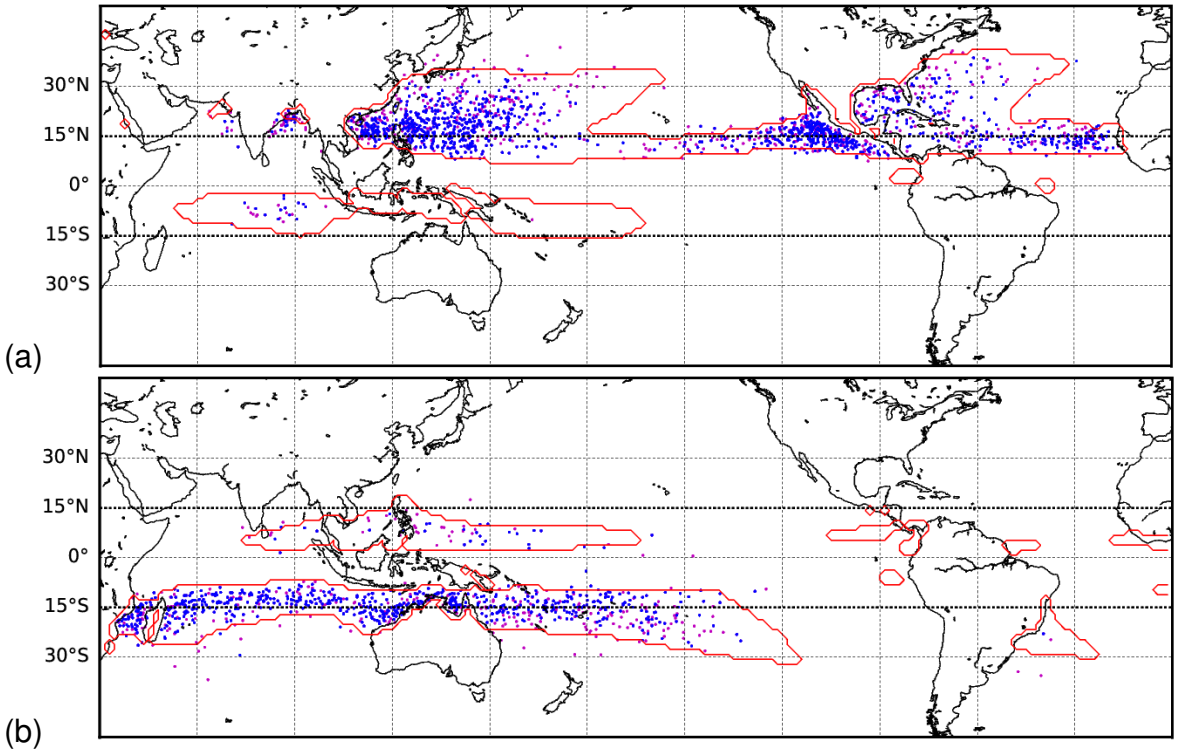

Figure 5: As in Fig. 4, but with regions with all four thresholds satisfied indicated by the red contour.

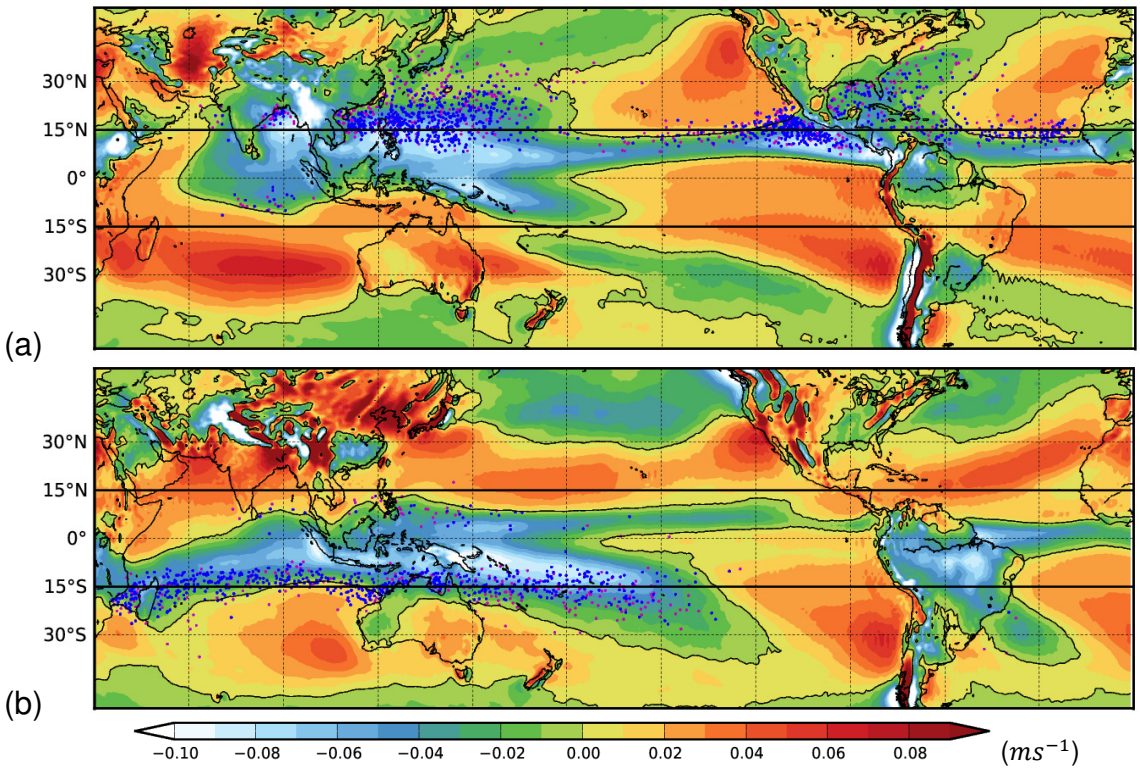

Figure 6: Summer season vertical velocity on the 500 hPa pressure level with OWZP detected TDs (purple) and TSs (blue), for (a) July—September (b) January—March, from ECMWF reanalyses (1979—2013).

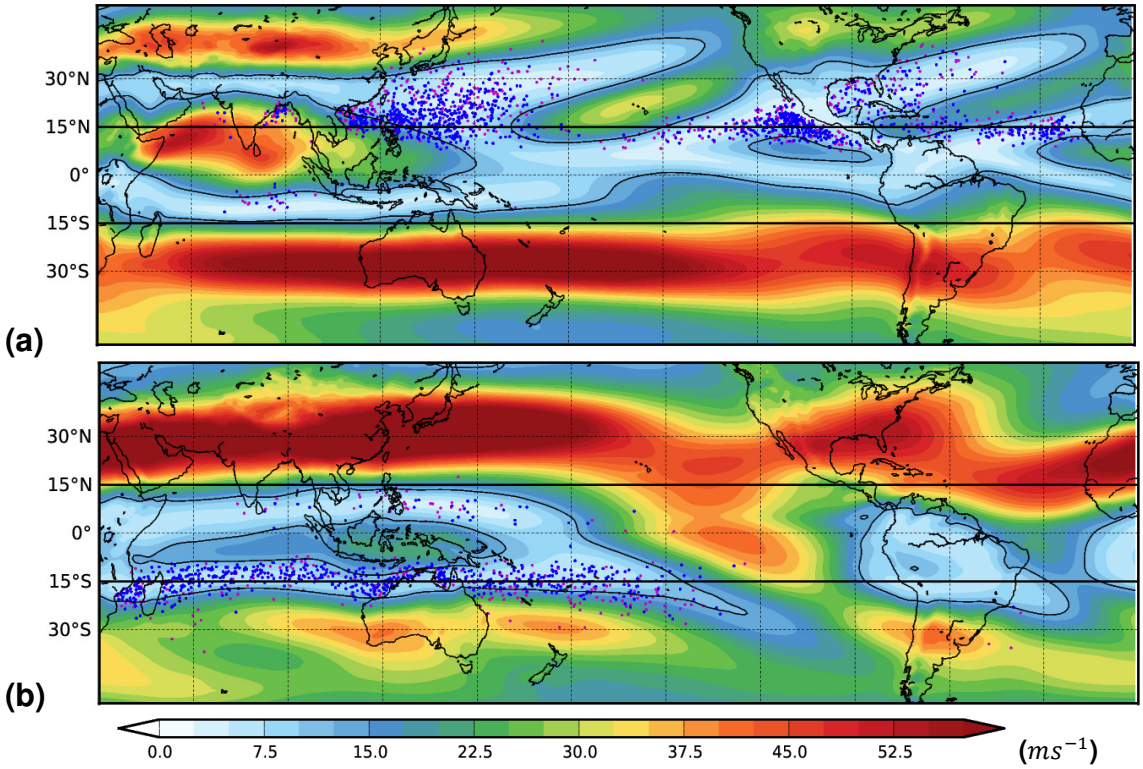

Figure 7: Summer season magnitude of the vector wind difference between 850 and 200 hPa horizontal winds (V_{sh}), for (a) July—September (b) January—March, from ECMWF reanalyses (1979—2013). The 12.5 ms^{-1} contour is included in black.

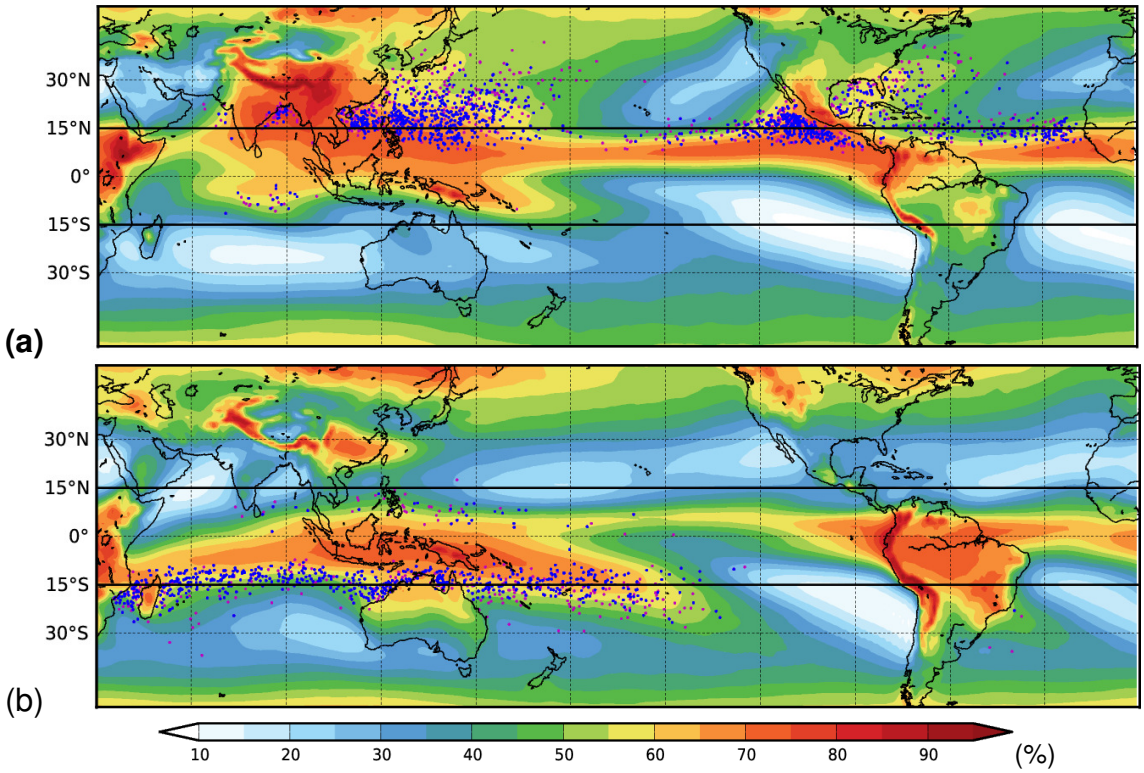

Figure 8: Summer season relative humidity on the 700 hPa pressure level, for (a) July—September (b) January—March, from ECMWF reanalyses (1979—2013).

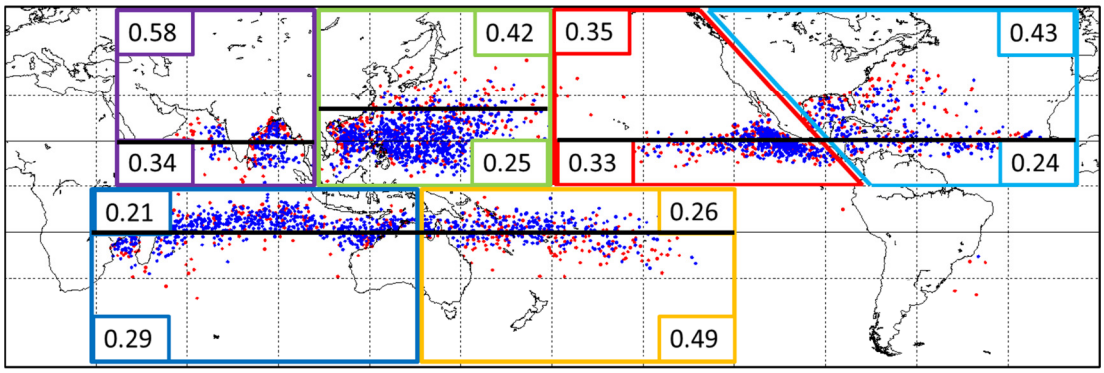

Figure 9: All season OWZP TD (red) and TS (blue) detections from 1979—2013 ERA-interim reanalysis data, with the TD failure rate fractions poleward and equatorward of a latitudinal dividing line listed for each TC basin. In the NW Pacific the dividing latitude is 25°. In all other basins it's 15°.

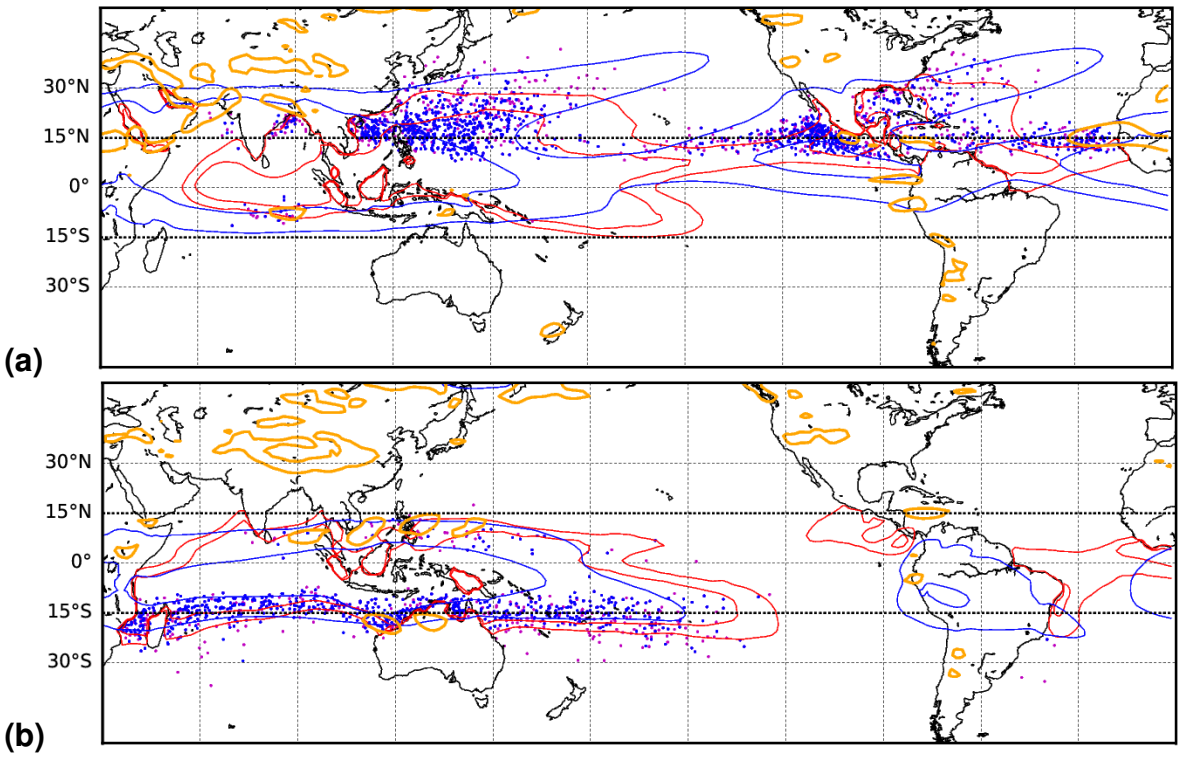

Figure 10: As in Figs 2—4 but for the thresholds used to define the low TD failure rate regions. $V_{PI} = 65, 75\ ms^{-1}$ (red), $V_{sh} = 10\ ms^{-1}$ (blue) and $\beta^* = 0$ (orange).

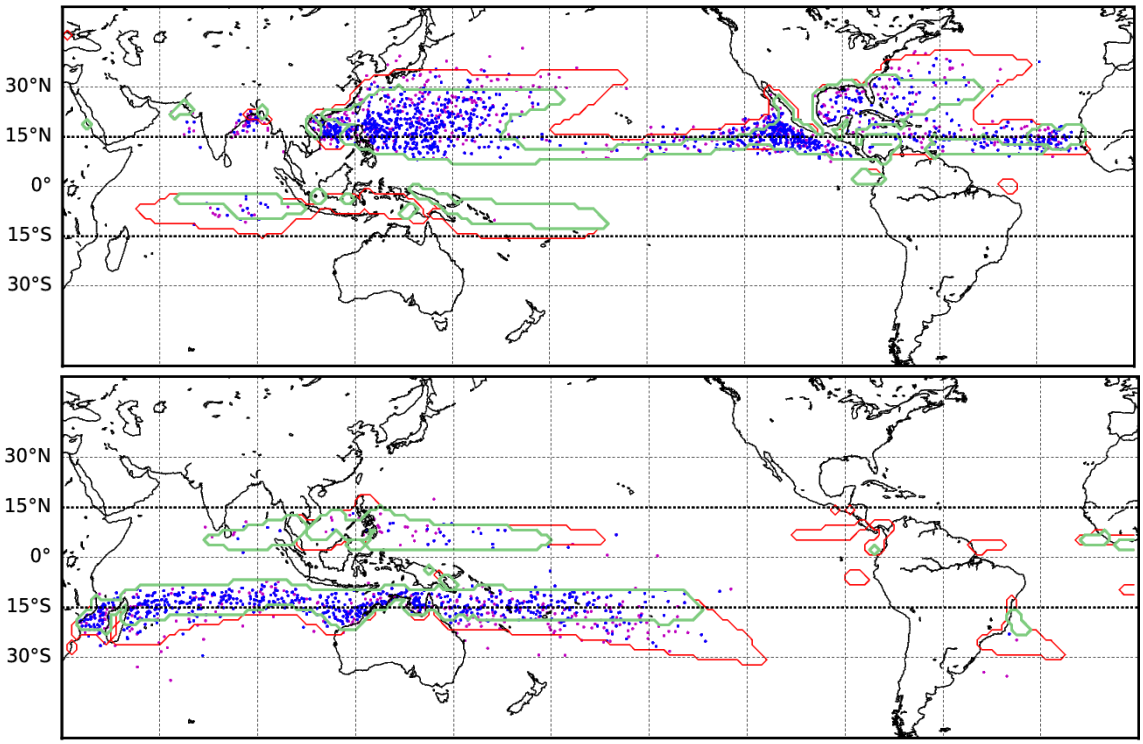

Figure 11: As in Fig. 5 but with the boundaries defining the low TD failure regions (green) added.